SAR Compliance Simulation Report for iPhones
V1.0.0

Model No.	FCC ID
A3081	BCG-E8688A
A3286	BCG-E8689A
A3287	BCG-E8690A
A3288	BCG-E8691A
A3082	BCG-E8692A
A3289	BCG-E8693A
A3290	BCG-E8694A
A3291	BCG-E8695A

Date of Simulation:
04/15/2024-06/15/2024
Location:
Apple Inc., Cupertino, CA, USA

Table of Contents

List of Figures:

List of Tables:

1 Introduction

This report demonstrates RF exposure compliance using SAR simulation for 2024 iPhone models (FCC IDs: BCG-E8688A, BCG-E8689A, BCG-E8690A, BCG-E8691A, BCG-E8692A, BCG-E8693A, BCG-E8694A, BCG-E8695A). The wireless power transfer (WPT) module on 2024 iPhones, in addition to being charged by a desktop and portable WPT charger (puck), also support WPT charging function at 360 KHz to charge accessories. This report presents the evaluation of SAR and E-field induced inside a human tissue when the iPhone is wirelessly charging potential external accessories.

To demonstrate RF exposure compliance for 2024 iPhones at 360 KHz operating frequency, as permitted by §2.1093 (certification for portable devices below 4 MHz), SAR numerical simulations are performed to demonstrate compliance to the 1.6 W/Kg localized 1-g SAR limit.

Currently, the charging session only occurs when the phone is connected to an AC power outlet. However, due to the potential apple accessories in future and the phone being held in place by magnets, it is envisioned that customers may use the charging function in a portable use condition, for example, charging the battery while making a call or texting. Therefore, to be conservative we evaluate iPhone WPT transmitter as a mixed mobile/portable device. Future designs and accessories may support true portable use condition, with the host-client pair able to be placed in a pocket or backpack. In those cases, a body-worn exposure assessment would be conducted.

The following sections describe the modeling, measured H-field, simulated H-field, and simulated SAR.

2   Wireless Power Transfer System

The wireless power transfer system consists of a transmitting coil with 13 turns and measures 9.06 uH nominally in free air. The coil is wound spirally and made of stranded wire. Below are the details of the Phone (Tx) coil which is used in all the iPhone models described in section 1 of the report.

Tx Coil Winding Type	Spiral, 1 Layer, Stranded Wire
Turns	13
Inner Radius	10.06 mm
Outer Radius	21.35 mm
Cross-section	Rectangular
Thickness	0.13 mm
Width	0.62 mm

Rx Coil Winding Type	Spiral, 1 Layer, Stranded Wire
Turns	11
Inner Radius	10.9 mm
Outer Radius	18.9 mm
Cross-section	Rectangular
Thickness	0.32 mm
Width	0.49 mm

Below are some key initial parameters used in the design that will be helpful in determining worst-case use for exposure: These are common to all the iPhone models described in section 1 of this report.

Table 1. Key design parameters

Item	Description
Max Power	7.5 W
Functional On-body max offset	Refer to the graph below*
Operating Frequency	$f_0 = 360$ kHz
Communications/Modulation Method	FSK -> Phone to Accessory ASK -> Accessory to Phone
Object Detection Mode	Magnetic + NFC

* Refer to antenna location file for all antennas in the phone, and how the WPT coil is separated from other antennas.

3 SAR Simulations Methodology

The following steps has been taken to show the validity of the model used for SAR Simulations:

1) EM Simulation:
   a. Import a CAD model that represents the actual product in the simulation tool.
   b. Define material properties inside the product based on vendor's inputs.
   c. Extract two-port network impedance matrix ([Z]) from the simulation.
2) Circuit Simulation:
   a. Include the impedance matrix in the wireless power transfer (WPT) circuit model.
   b. Run circuit simulation and extract coils' current waveforms.
3) Field Calculations:
   a. Use the current waveforms to drive the EM simulation model.
   b. Calculate H-field from the simulation.
4) Validate Simulation Model:
   a. Measure H-field, and compare with simulation result
   b. Perform full uncertainty analysis
   c. Once a correlation is established, and model's accuracy is verified, this model will be used for computational exposure assessments (e.g., SAR simulations).

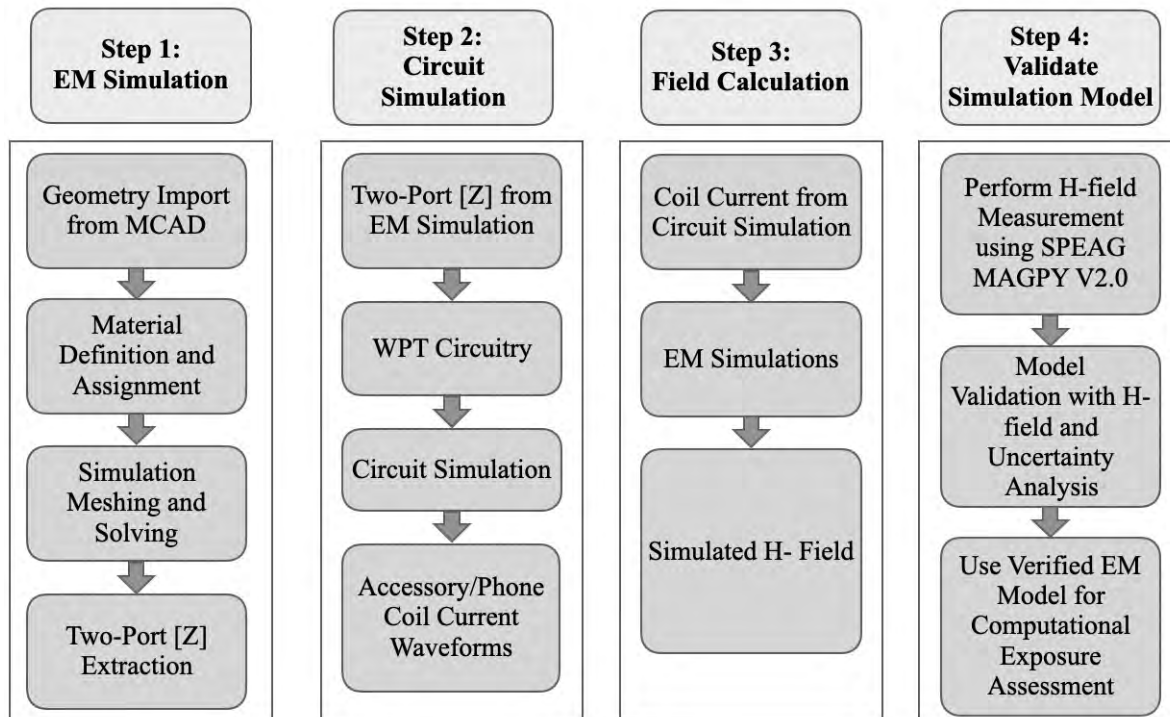The entire workflow is summarized and shown in Fig. 1.

Figure 1: Model validation workflow for computational exposure assessment.

4 H-field Simulations for Transmitter

The Electromagnetics simulations are conducted using commercially available software ANSYS HFSS. To validate the simulation model, H-field measurements are made on the EUT (as explained above) and compared to the simulated model results. The validated model is then used for SAR simulations.

SPEAG Magnetic Amplitude and Gradient Probe System (MAGPy) V2.0 probe shown in Fig. 2 is used to measure the H-field. This probe consists of 24 small loop sensors arranged on the corners of a 22mm cube used for measuring H-field amplitude and gradient. The lower measuring loops are 7.5mm from the probe tip enabling a closer measurement to the electromagnetic source. The probe also has two dipoles and a monopole to measure the E- field. Probe specifications are described in Table 2.

Figure 2: SPEAG MAGPy V2.0 Measurement probe

Table 2. Probe Specifications:

Model	MAGPy V2.0
Frequency	3 KHz – 10 MHz
Measurement Center	18.5 mm from the probe tip
Dimensions: (H-field sensor loop size) (E-field sensor arm length) (Overall Diameter)	1 cm² 50 mm 60 mm
Dynamic Range	0.08 to 2000 V/m for Electric field 0.1 to 3200 A/m for Magnetic field
Measurement Uncertainty (Extended $k=2$)	1.3 dB
Application	Electric and Magnetic field measurement

For the simulation-measurement correlation study, the direct exposure case where only the iPhone (TX) is present is chosen. The measurement setup is shown in Fig. 3. As shown in the measurement setup, the center of probe coils is 18.5 mm away from the true 0 mm touch position and lower four sensor are 7.5mm away. Following procedure was used to compute the averaged fields from simulation results for correlating with measured data: The volumetric H-field is exported from HFSS and post-processed using a MATLAB script to include the SPEAG MAGPY V2.0 probe averaging effect. The SPEAG MAGPY V2.0 probe has 8x3 internal loops. These loops measure H-field by integrating it over their effective aperture area. The script will apply this integration over the exported volumetric H-field. Worth mentioning that the script does not consider any potential loading effect that the probe may have on the DUT, including mutual interaction with the DUT coils. To our experience, this mutual interaction is partially responsible for the discrepancy between the simulation and measurement results when the probe is touching the DUT. Detailed description of the post-processing is also shown in Fig. 4.
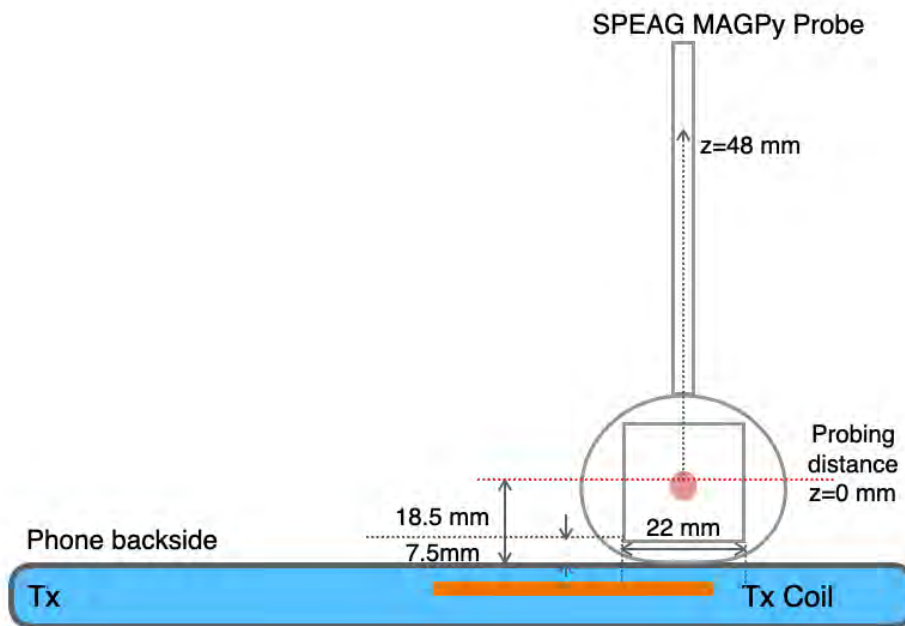
Figure 3: H-field measurement setup for direct exposure case
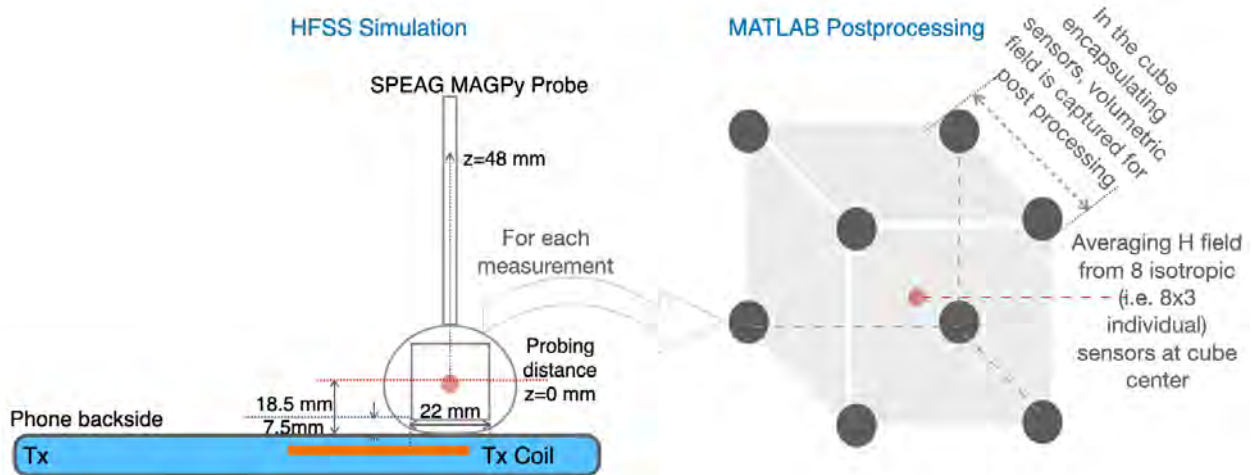
Figure 4: Post-processing using MATLAB script: Volumetric field data is exported from HFSS and processed to include SPEAG MAGPY V2.0 probe effect.

Simulation model and measurements correlation is performed at a vertical distance away from the DUT and the probe is moved vertically in Z direction from 0 mm (probe center) with the step size of 2 mm till 25 measurements are taken.
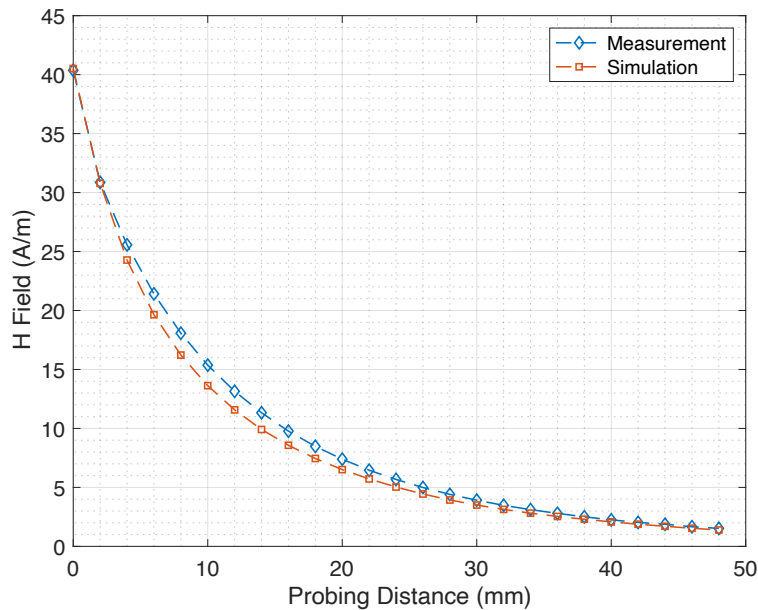
Figure 5: Simulation Vs Measured H-field comparison for direct exposure case

The above Fig. 5 shows good correlation between the measurements and simulations. At distance very close to the DUT, simulations are little more conservative than measurements. This validated simulation model is then used for SAR simulations in the next sections.

5 SAR Simulations

The validated simulation model is used for SAR calculations with a phantom added in contact with the EUT. The simulations are computed on a 40 core CPU server with an available RAM of 2Terabytes. For this simulation, the model run takes approximately 6 hours to complete.

The following steps are used for accurate SAR calculations:
1) Elliptical phantom used in body exposure measurements is commercially available from SPEAG: Outer Dimensions of 600mm x 400mm x 150mm.
2) Homogeneous tissue material is used as liquid for desired frequency.
3) Power loss in phantom is calculated.
4) Divide power loss by mass density to calculate SAR.

$$SAR = \frac{P_l}{\rho}$$

P_l = Power loss density

ρ = Mass density

5) Point SAR is averaged over 1g or 10g tissue.
6) For SAR simulations, mass density of 1000 Kg/m^3 is used for the Phantom.

Human Tissue Material Properties at 360 kHz:
The worst-case scenario has been identified to be when a user is holding the device in hand and taking a call or holding the phone on their body while charging. The electrical properties for body and hand layers are shown below [ref. 3-7]. Since the SAR phantom is homogenous, using the layers' properties, the worst-case scenario is selected and applied for the phantom properties. Therefore, for the SAR simulations, the phantom that has conductivity of 0.5 and permittivity of 5016 at the 360 kHz operating frequency is used.

Electrical Properties:
Based on our research this is what we recommend for εr and sigma (σ) values for body layers

Tissue	Thickness (mm)	Permittivity	Conductivity (S/m)
Skin	3	5016	0.16
Muscle	9	4666	0.5
Bone	20	1414	0.165
Worst case	100	5016	0.5

Based on our research this is what we recommend for er and sigma values for hand layers

Tissue	Thickness (mm)	Permittivity	Conductivity (S/m)
Skin	2	5016	0.16
Muscle	2	4666	0.5
Bone	15	1414	0.165
Worst case	100	5016	0.5

Bone (Cancellous)
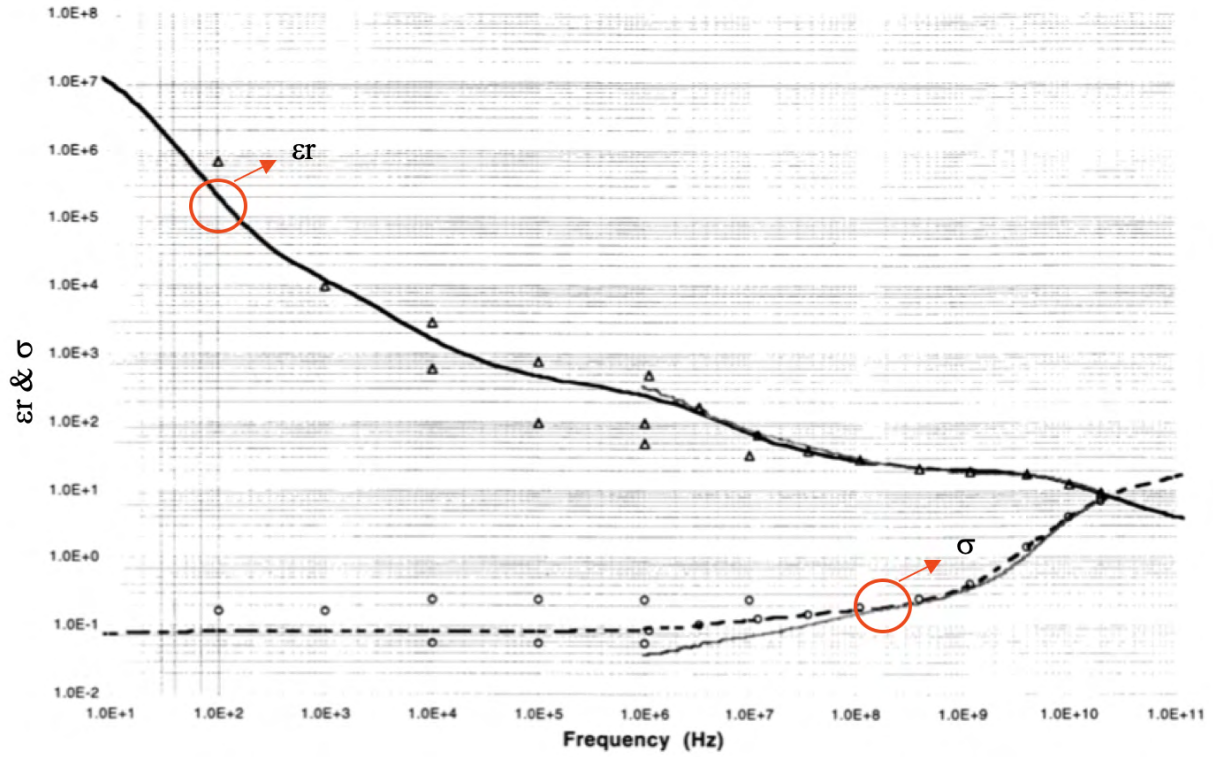
Muscle
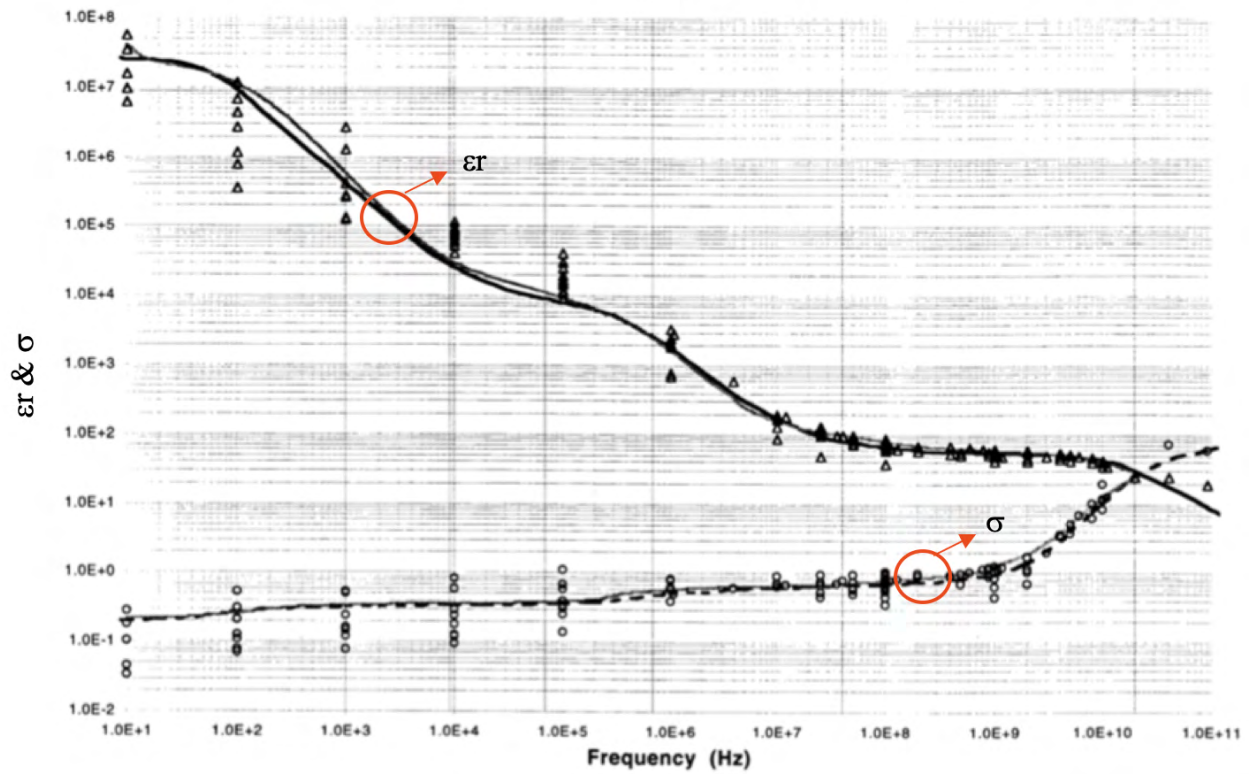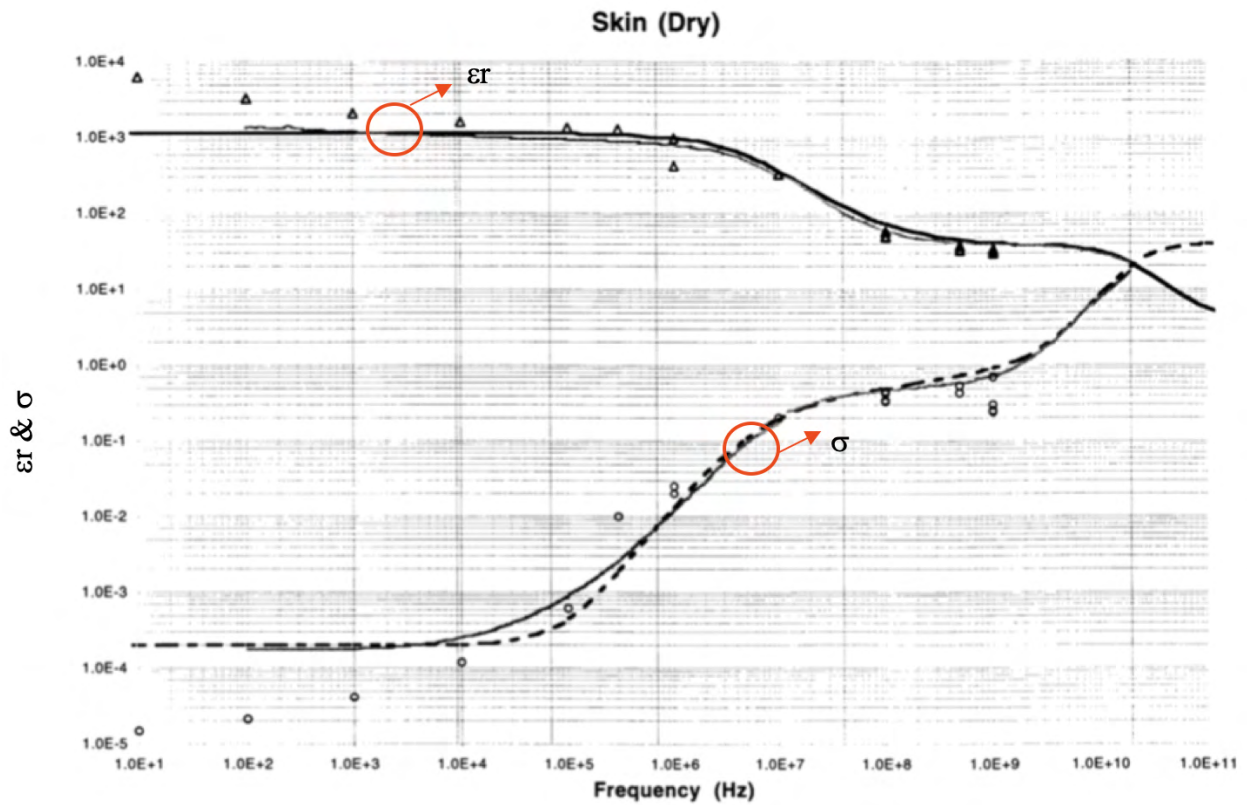
Mesh Adaptation:

HFSS adapts the mesh based on field strength. It is important to ensure the mesh is refined to capture SAR accurately. This can be done by using adaptive meshing available in HFSS and mesh refinement process is described in Fig. 6.

Figure 6: Initial mesh generation and then refinement through adaptive meshing technique in HFSS.

SAR Results:

Two exposure cases were selected for SAR investigation. Considering that the phantom can be in contact with the phone or accessory, there is a total of four scenarios.

5.1 Exposure Cases:

Exposure Case 000 (a): Nominal configuration with perfect alignment and phantom placed above the transmitting unit.
Exposure Case 000 (b): Nominal configuration with perfect alignment and phantom placed below the receiving unit.
Exposure Case 202 (a): Misaligned configuration with the worst-case alignment and phantom placed above the transmitting unit.
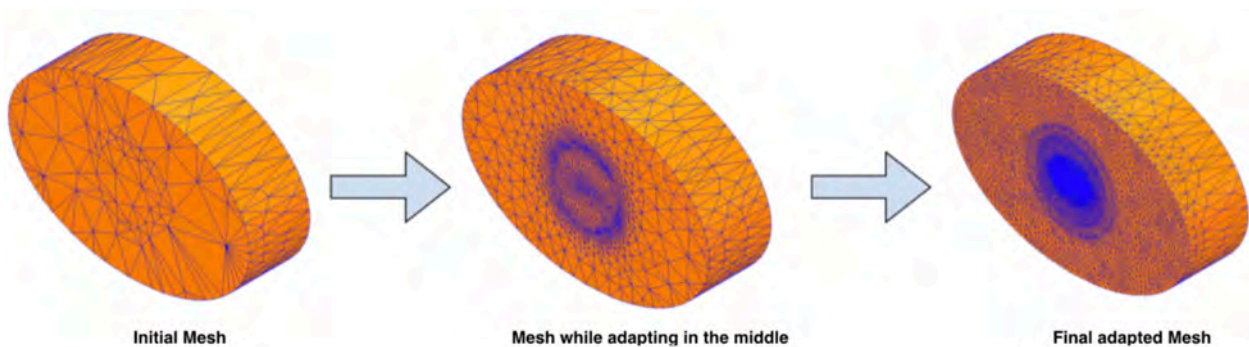**Exposure Case 202 (b):** Misaligned configuration with the worst-case alignment and phantom placed below the receiving unit.

For all the exposure cases, dielectric properties (conductivity and permittivity) used for the phantoms are fixed as (permittivity: 5016, conductivity: 0.5).
The coil properties are also fixed, transmitting coil with 13 turns and measures 9.06 uH nominally in free air. The receiver coil consists of 11 turns and measures 7.5 uH nominally in free air. Both coils are wound spirally.
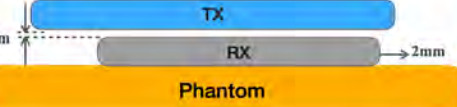
The following outputs are calculated and reported in the Table:
   a. Peak spatial 1-g average SAR in tissue.
   b. Peak spatially averaged electric field in tissue. Electric field is spatially averaged in a contiguous tissue volume of 2 mm by 2 mm by 2 mm.

The simulation results for the use cases and direct exposure scenarios are listed in the Table 3 below:

Table 3: Averaged 1-g SAR and Peak Spatial Average E-field (inside Phantom) simulation results for the nominal use cases

Exposure Case	Description	Peak Spatial Average SAR (W/Kg) Averaged over 1 gram	Peak Spatial Average E-field (V/m) Averaged over 2x2x2 mm^3
Case 000 (a)		0.000000006	0.01
Case 000 (b)		0.00000007	0.02
Case 202 (a)		0.00000006	0.02
Case 202 (b)		0.0000007	0.06

SAR plot is shown in Fig. 7 (a) for Case202(b). The peak spatial 1-g average SAR is 0.0000007 W/kg.
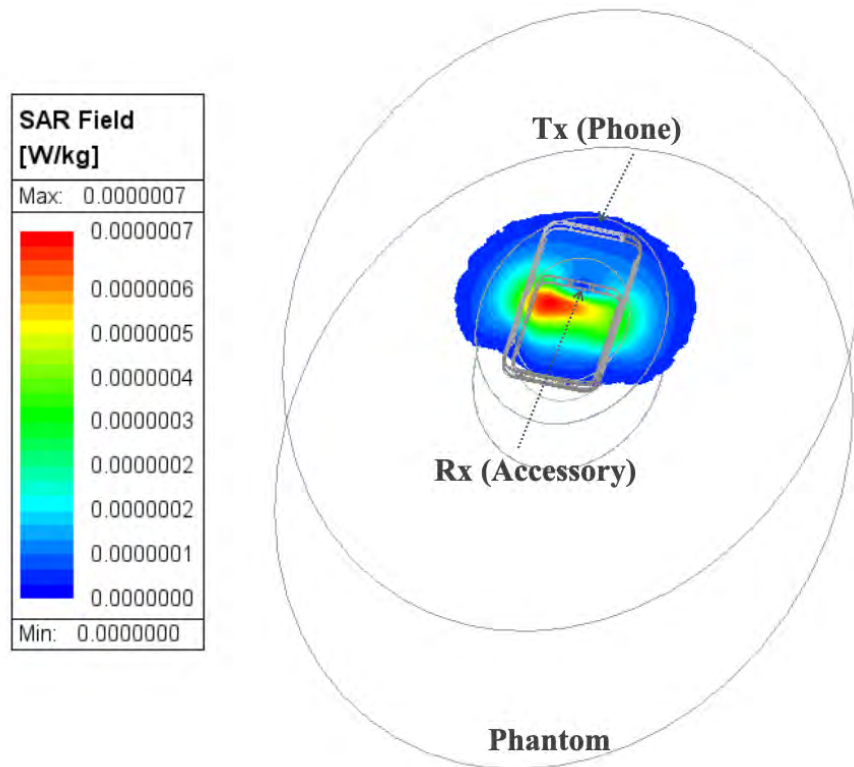
(a) Full view of average SAR plot for Case 202 (b)

The side view is also presented as shown in Fig. 7 (b) below.
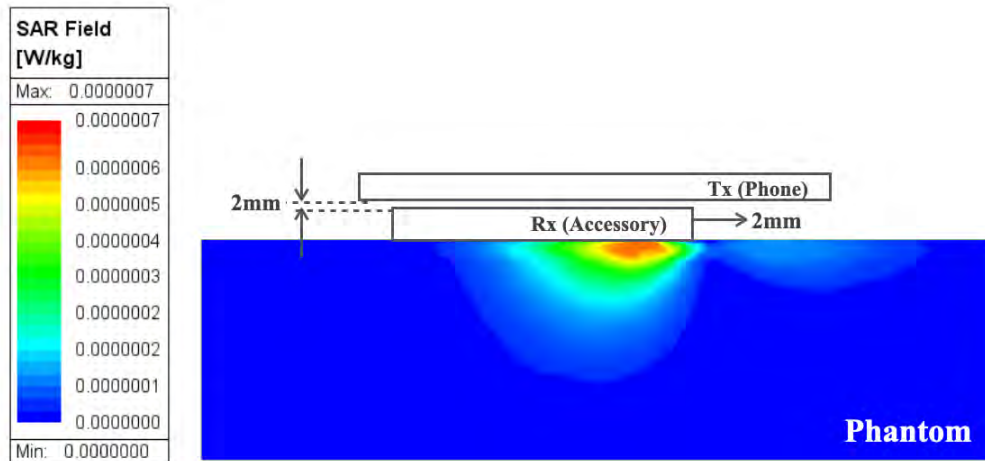
(b) Side view of average SAR plot for Case 202 (b)

Figure 7: Spatial 1-gram average SAR for Case 202 (b), (a) full view, (b) side view.

5.2 Additional Exposure Cases:

In addition, two corner cases were also investigated that are not likely to happen in normal application when the iPhone (Tx) is in direct contact with the Phantom with no accessory present is also investigated.

Direct Exposure (unrealistic) Case 1(a): with receiver absent and the phantom facing towards the phone (Tx) coil.
Direct Exposure (unrealistic) Case 1(b): with receiver absent and the phantom facing away from the phone (Tx) coil.

Peak 1-g averaged SAR and E-field inside the Phantom for the Direct exposure cases are shown below.

Table 4. Averaged 1-g SAR and Peak Spatial Average E-field (inside Phantom) simulation results for direct exposure.

Exposure Case	Description	Peak Spatial Average SAR (W/Kg) Averaged over 1 gram	Peak Spatial Average E-field (V/m) Averaged over 2x2x2 mm^3
Case 1(a)	Phantom / TX / Tx Coil	0.0000007	0.07
Case 1(b)	TX / Tx Coil / Phantom	0.0174	13.90

SAR plot is shown in Fig. 8 for Direct Exposure (unrealistic) Case 1(b). The peak spatial 1-g average SAR is 0.0174 W/kg.
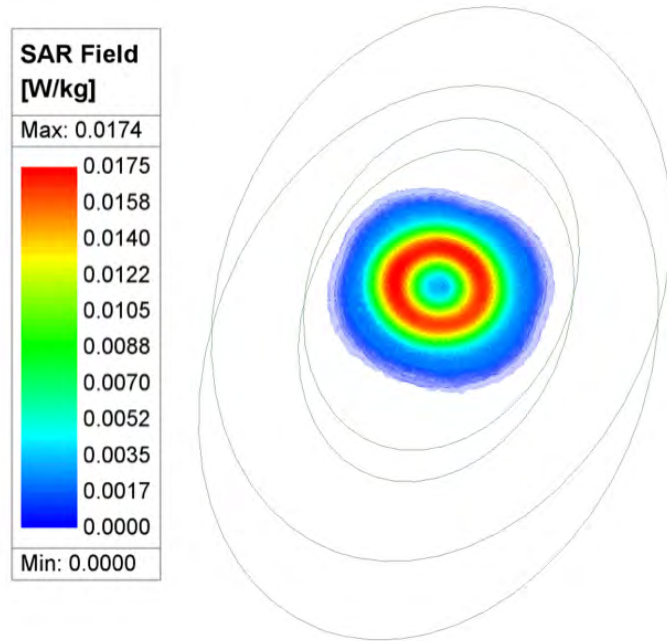
(a) Average SAR plot for Direct Exposure Case 1(b)
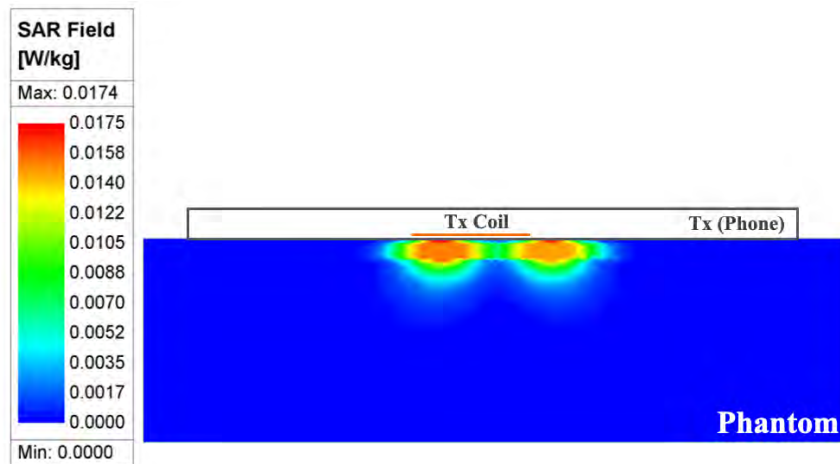
(b) Side view of average SAR plot for Direct Exposure Case 1(b)

Figure 8: Spatial 1-gram average SAR for Case 1 (a), (a) full view, (b) side view

E-field distribution inside the phantom for the Case1(a) is shown below. Please note that the value reported in the table above was averaged over a cube of 2mmx2mmx2mm and that explains why the value is lower than the peak E-field in this plot.
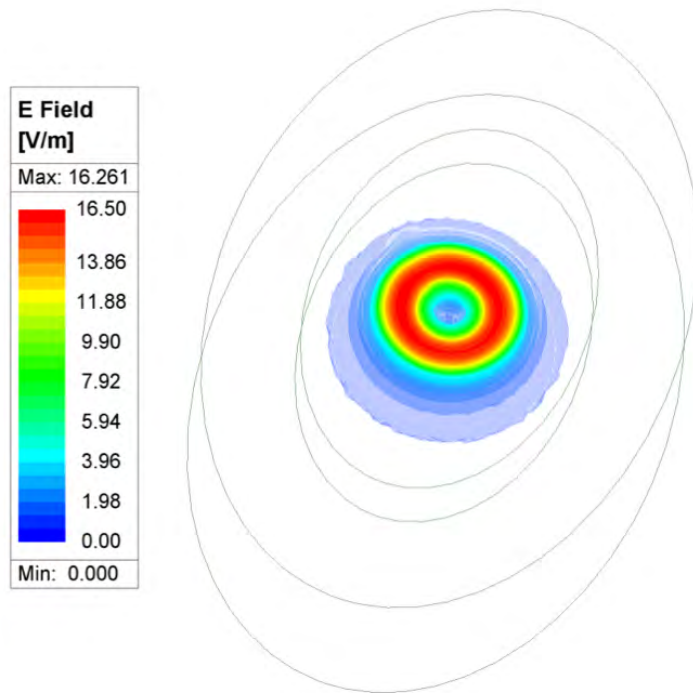
Figure 9: Peak E-field distribution inside Phantom for Direct Exposure Case 1(b)

6   Impact of Housing Size

The iPhones for 2024 will have two different sizes as summarized in the sketched outlines below. Model No.s, FCC IDs: A3081, BCG-E8688A; A3286, BCG-E8689A; A3287, BCG-E8690A; A3288, BCG-E8691A on which the detailed analysis was performed in the earlier sections have lower-size dimensions. The larger form factor is for the following Phones: Model No.s, FCC IDs - A3082, BCG-E8692A; A3289, BCG-E8693A; A3290, BCG-E8694A; A3291, BCG-E8695A.
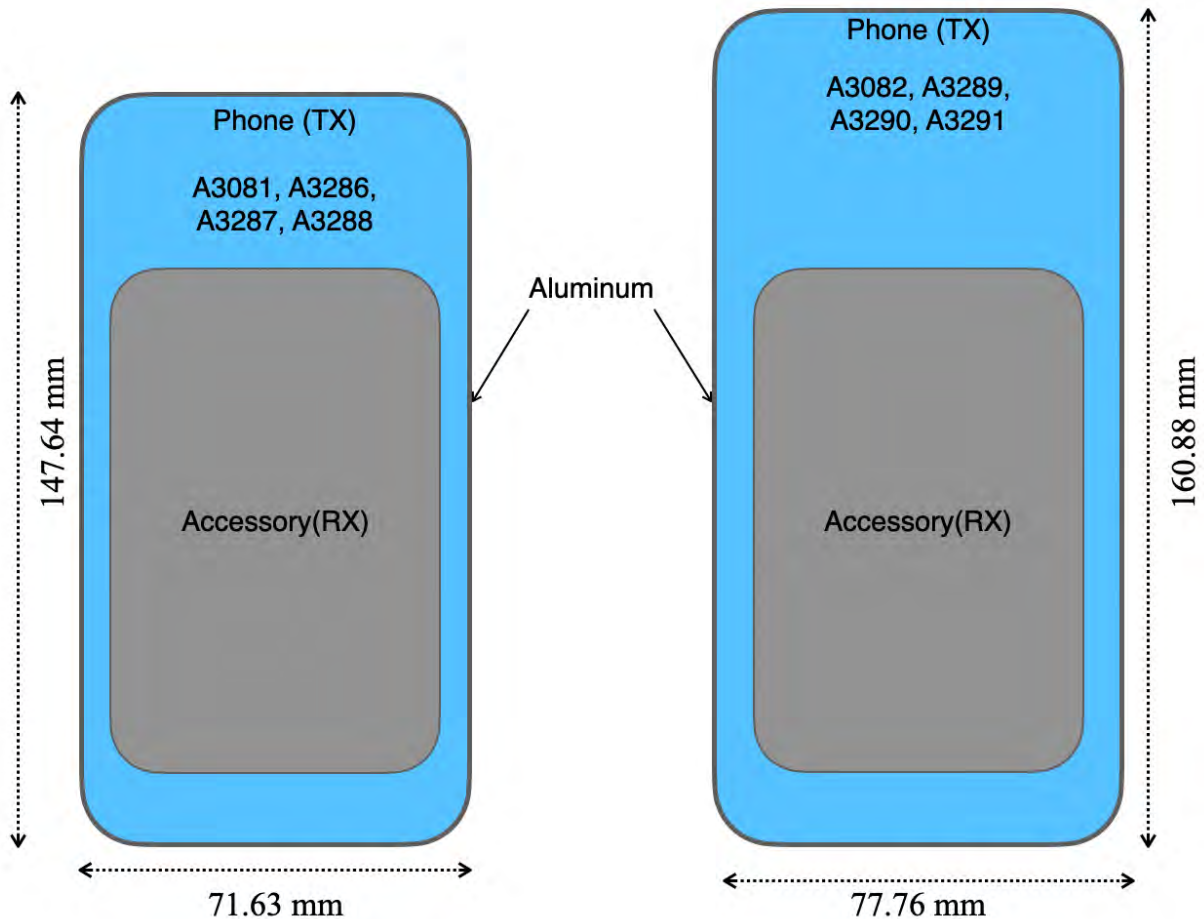
Figure 10: Comparison of 2024 iPhone Dimensions for A3081, A3286, A3287, A3288 and A3082, A3289, A3290, A3291.

They share common material for the back of the phone and same material (Aluminum) is used for housing as well. In this section, we used the worst-case orientation (202-b and 1002-b) from the initial analysis done; to study how the SAR and E-field changes with different housing sizes. The table below summarizes the results, and the SAR plots are shown for each size.

Table 5. Comparison of Average SAR and Peak Spatial Average E-field for different housing sizes

Model number	Housing Size (mm)	Peak Spatial Average SAR (W/Kg) Averaged over 1 gram	Peak Spatial Average E-field (V/m) Averaged over 2x2x2 mm^3
A3081, BCG-E8688A; A3286, BCG-E8689A; A3287, BCG-E8690A; A3288, BCG-E8691A	71.63x 147.64	0.0000007	0.06
A3082, BCG-E8692A; A3289, BCG-E8693A; A3290, BCG-E8694A; A3291, BCG-E8695A	77.76 x 160.88	0.0000004	0.050

From the above table, we can see that housing size has very less impact on the SAR and E-field values.
The SAR plots comparison for different form factors is shown below.

Table 6. Peak Spatial Average SAR (W/Kg) plots for different housing sizes

Model number	Housing Size (mm)	Peak Spatial Average SAR (W/Kg) Averaged over 1 gram
A3081, BCG-E8688A; A3286, BCG-E8689A; A3287, BCG-E8690A; A3288, BCG-E8691A	71.63x 147.64	

A3082, BCG-E8692A; A3289, BCG-E8693A; A3290, BCG-E8694A; A3291, BCG-E8695A	77.76 x 160.88	
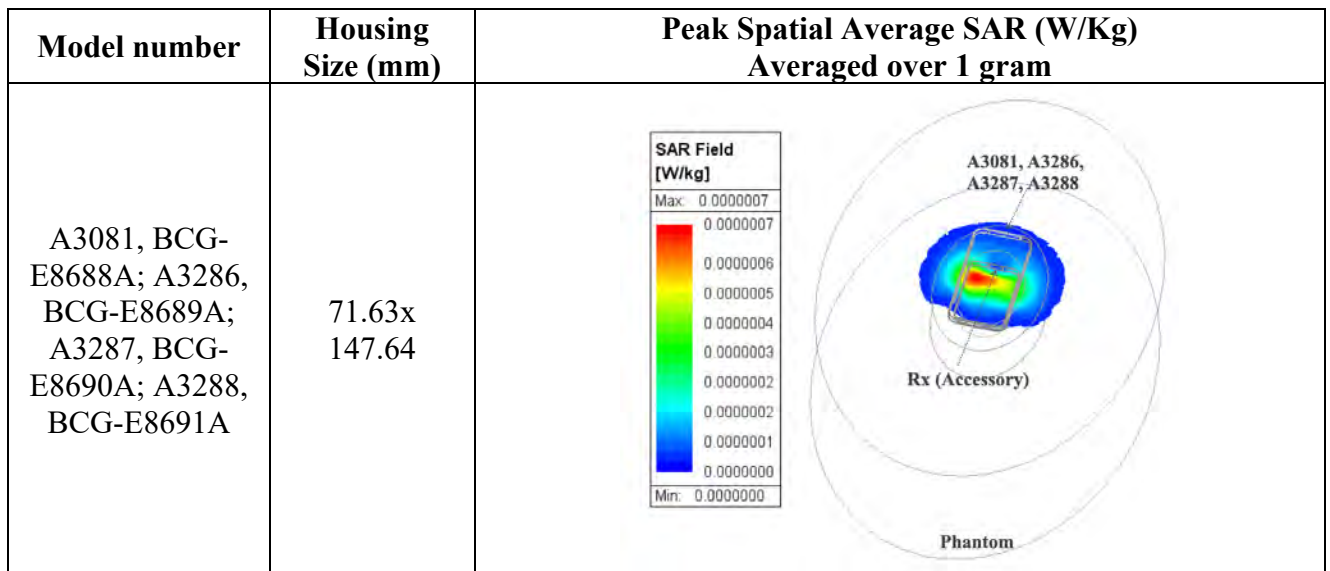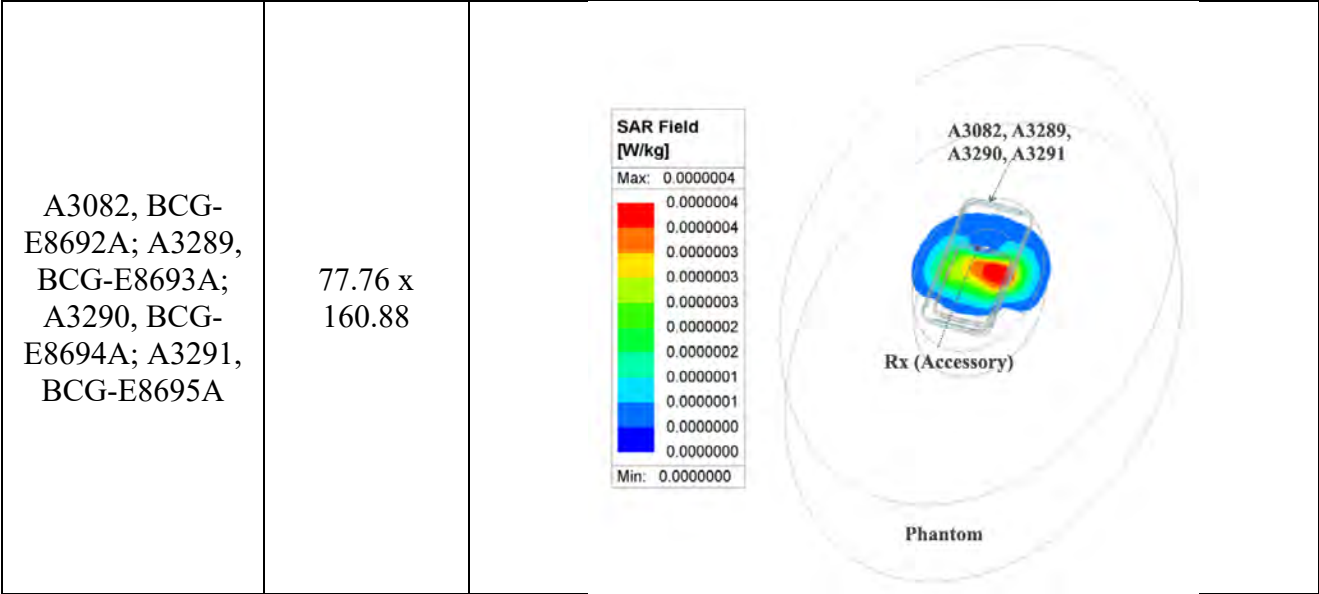
Summary

Based upon the above results, the accuracy of the SAR simulations is demonstrated by correlating H-field measurements to simulations. The validity of using this modeling and SAR computational method hence is established for iPhone models FCC IDs: BCG-E8688A, BCG-E8689A, BCG-E8690A, BCG-E8691A, BCG-E8692A, BCG-E8693A, BCG-E8694A, BCG-E8695A. Among, the exposure cases, the highest peak spatial 1-gram averaged SAR of 0.000007 W/Kg and the highest peak spatial average E field (i.e., averaged over a cube of 2 mm x 2 mm x 2 mm) of 0.063V/m, is observed when the "Accessory" and the phone are misaligned with vertical separation.

Overall, the SAR is significantly lower than the SAR limit of 1.6 W/Kg (below 0.01% of the actual SAR limit). Therefore, we respectfully request that the allowance to use of this model to demonstrate RF Exposure compliance for Apple's proposed WPT products.

Annex A: Specific information for SAR computational modelling

1) Computation Resources

The models were simulated on a 40 core CPU server with an available RAM of 2 Terabytes. Each model variation took around 6 hours to complete. Based on the simulation profile, the minimum resources needed to finish these simulations will be approximately 8 core CPU with 512 GB of RAM. Using the minimum requirements simulation will likely take more time than 12 hours.

2) Algorithm implementing and validation

This section is divided into two parts. The code performance validation provides methods to determine that the finite-element algorithm in HFSS has been implemented correctly and works accurately within the constraints due to the finite numerical accuracy. It further determines the quality of absorbing boundary conditions and certain parts of the post processing algorithms that are part of HFSS. The second part has few canonical benchmarks. All benchmarks can be compared to analytical solutions of the physical problem or its numerical representation. The methods characterize the implementation of the finite-element algorithm used by HFSS in a very general way. They are defined such that it is not possible to tune the implementation for a particular benchmark or application without improving the overall quality of the code.

2.1) Code performance validation

2.1.1) Propagation homogeneous medium

A straight rectangular waveguide with ports on both ends is well suited as a first test of an implementation of the Finite-Element Method used by HFSS. The waveguide has a width of 20 mm, a height of 10 mm and a length of 300 mm. The waveguide is filled homogeneously with a material which, in three separate simulations, shall assume the following properties:

    i. $\varepsilon r = 1$, $\sigma = 0$ S/m;
    ii. $\varepsilon r = 2$, $\sigma = 0$ S/m;
    iii. $Re(\varepsilon r) = 2$, $\sigma = 0.2$ S/m.

To verify that the mesh used by HFSS is independent of orientation, the waveguide has been rotated so that it is not parallel with any principal coordinate plane (XY, XZ, YZ). The waveguide is driven in the TE10 mode at 10 GHz. Reported are the magnitudes of S21 and S11, as well as the values of the real and imaginary parts of the propagation constant γ. The table 7, below provides the reference values [B1], acceptable result criteria, as well as the simulated results.

Table 7: Criteria for the waveguide evaluation

Re(ε_r)	1	2	2
σ	0	0	0.2
|S21| reference value	1	1	$8.7 \times 10\text{-}5$
Criterion for |S21|	≥ 0.9999	≥ 0.9999	$\pm 5 \times 10\text{-}6$
|S21| simulated results	1	1	$8.7 \times 10\text{-}5$
|S11| reference value	0	0	0
Criterion for |S11|	≤ 0.003	≤ 0.003	≤ 0.003
|S11| simulated results	0	0	0
Re(γ) reference value	0	0	31.17 m-1
Criterion for Re(γ)	± 0.1 m-1	± 0.1 m-1	$\pm 2\%$
Re(γ) simulated results	0	0	31.17
Im(γ) reference value	138.75 m-1	251.35 m-1	253.28 m-1
Criterion for Im(γ)	$\pm 2\%$	$\pm 2\%$	$\pm 2\%$
Im(γ) simulated results	138.75	251.35	253.28

As is seen in the above table, HFSS easily meets the criteria for properly and accurately calculating the waveguide problem.

2.1.2) Planar dielectric boundary

In order to test the reflection of a plane wave by a dielectric boundary, a rectangular waveguide can again be used. It is well known that the TE10 mode can be thought of as a superposition of two plane waves [1]. Each wave's direction of propagation makes an angle θ with the axis of the wave guide, given by

$$\cos^2\theta = 1 - (c/2af)^2 \tag{1}$$

where c is the speed of light, a is the width of the wave guide and f is the frequency. Assuming the axis of the waveguide is the Z axis and assuming the waveguide is filled with vacuum for Z>0 and filled with dielectric 1 with complex relative permittivity ε_r for Z<0, Fresnel reflection coefficients for the TE and the TM cases, defined as ratios of electric field strengths, are given by [2]

$$R^{TE} = (k_{0,z} - k_{1,z}) / (k_{0,z} + k_{1,z}) \tag{2}$$

$$R^{TM} = (\varepsilon_r k_{0,z} - k_{1,z}) / (\varepsilon_r k_{0,z} + k_{1,z}) \tag{3}$$

where $k_{0,z}$ and $k_{1,z}$ denote the z component of the propagation vector of the plane wave in vacuum and in the dielectric, respectively. They can be evaluated through

$$k_{0,z} = k_0 \cos\theta \tag{4}$$
$$k_{1,z} = k_0 \sqrt{(\varepsilon_r - \sin^2\theta)} \tag{5}$$

Finally, ε_r is complex and is given by

$$\varepsilon_r = Re(\varepsilon_r) - j\sigma/(2\pi f\varepsilon_0) \tag{6}$$

where $Re(\varepsilon_r)$ denotes the real part of the relative permittivity and σ is the conductivity of the medium.

For this test, a 20 mm × 10 mm waveguide with a length of 60 mm, as shown in Figure 11, was created. The top half was filled with vacuum and the bottom half with dielectric.
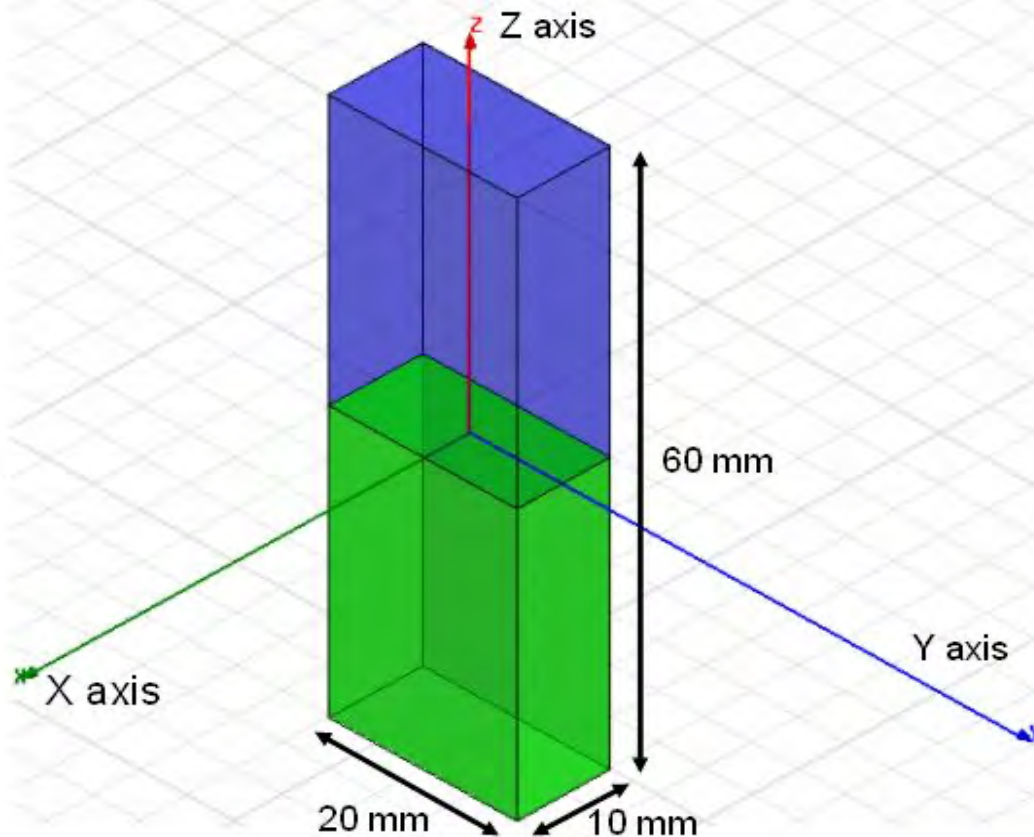

Figure 11: Waveguide filled half with vacuum and half with dielectric

In one copy of the model, all side walls were lossless metal, such that the dominant mode is the TE10 mode with propagation constant 138.75 m-1 at 10 GHz and represents the TE case in the reflection analysis. In the other copy of the model, the side walls that are parallel to the YZ plane were perfect magnetic conductors while the other walls were perfect electric conductors, such that the second mode (after a TEM mode which won't be used in this test) has propagation constant 138.75 m-1 at 10 GHz and represents the TM case in the reflection analysis.

Before simulation, the waveguides were rotated over an arbitrary angle such that no face is parallel with any coordinate plane. The waveguides were driven at 10 GHz in the proper mode. In doing so, it is good practice to calculate all propagating modes, but the coupling between modes is expected to be negligible. Simulations were run for the cases of lossless and lossy dielectric as shown in Table 8. For the HFSS to pass the test, according to IEC 62704-1, the results need to be within 2% of the analytical values given in Table 8.

Re(εr)	σ (S/m)	RTE	RTE- Simulated	RTM	RTM - Simulated
4	0	0.4739	0.4739	0.1763	0.1763
4	0.2	0.4755	0.4755	0.1779	0.1779
4	1	0.5105	0.5105	0.2121	0.2121

As can be seen in above table, HFSS produces results that are identical to the analytical results.

2.2) Canonical Benchmarks

The results for few low frequency benchmarks are summarized below. These benchmarks were used to validate the accuracy of the tool at low frequencies:

2.2.1) Dipole Antenna:
The following parameter were used in the dipole antenna to resonate at 400KHz.
Dipole length: 375 meters
Feed gap: 2.5 meters
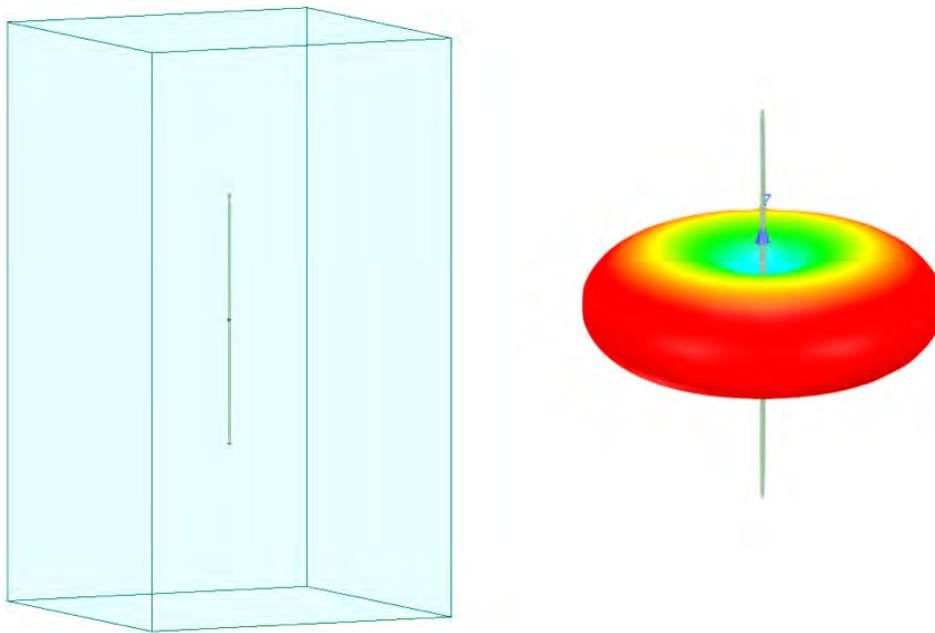Dipole Diameter: 5 meters

Figure 12: Dipole Antenna Model

The document IEC 62704-4 2020 was referenced to compare the tables. Two computation methods were demonstrated as shown below to show the validity of the model.

Table 9: Simulated dipole using FEM.

Quantity	Simulated Results	Tolerance	Satisfactory
Re(Z) @400 kHz	98.34 Ω		
Im(Z) @400 kHz	49.79 Ω		
Re(Z) @320 kHz	41.95 Ω	25 Ω < Re(Z) < 50 Ω	Yes
Im(Z) @320 kHz	-90.30 Ω	-50 Ω < Im(Z) < -100 Ω	Yes
Re(Z) @360 kHz	63.90 Ω	50 Ω < Re(Z) < 75 Ω	Yes
Im(Z) @360 kHz	-20.45 Ω	-25 Ω < Im(Z) < 0 Ω	Yes
Resonance Frequency Im(Z)=0	371.73 kHz	360 kHz < 380 kHz	Yes
Maximum power budget error	0.74 %	< 5 %	Yes

Table 10: Simulated dipole using MoM.

Quantity	Simulated Results	Tolerance	Satisfactory
Re(Z) @400 kHz	96.63 Ω		
Im(Z) @400 kHz	46.85 Ω		
Re(Z) @320 kHz	42.80 Ω	25 Ω < Re(Z) < 50 Ω	Yes
Im(Z) @320 kHz	-93.09 Ω	-50 Ω < Im(Z) < -100 Ω	Yes
Re(Z) @360 kHz	64.14 Ω	50 Ω < Re(Z) < 75 Ω	Yes
Im(Z) @360 kHz	-22.29 Ω	-25 Ω < Im(Z) < 0 Ω	Yes
Resonance Frequency Im(Z)=0	372.77 kHz	360 kHz < 380 kHz	Yes
Maximum power budget error	0.71	< 5 %	Yes

2.2.2) Toroid Inductor:

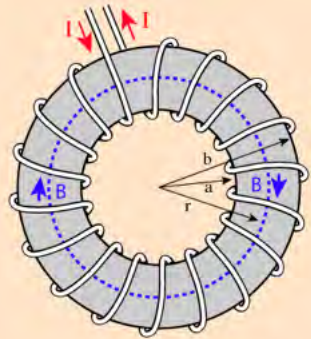The parameters of the toroid were chosen to be

N = 20

A = 6.35e-4 m^2

R = 0.0263 m

ur = 64

The formula below results in an inductance of 139 uH. The model created in HFSS resulted in an inductance of 138.06 uH at 1 MHz [ref 9].

Figure 13: Toroid Model

2.2.3) Circular coil parallel to a flat, homogeneous phantom.:

The following benchmark is implemented using Equations 1-4 of the referenced Chen et al. (2014) paper. The analytical calculations using the reference resulted in 1.6 V/m, which matches the HFSS result shown in Figure 15.

Below is the coil and phantom parameters:

Coil Diameter: 50 mm
Number of Turns: 10
RMS Current: 0.707 A (Peak current = 1 A)
Frequency: 100 kHz
Coil-to-Body Distance: 5 mm
Tissue Conductivity: 0.05 S/m
Tissue Permittivity: 1120
Phantom radius: 84 mm
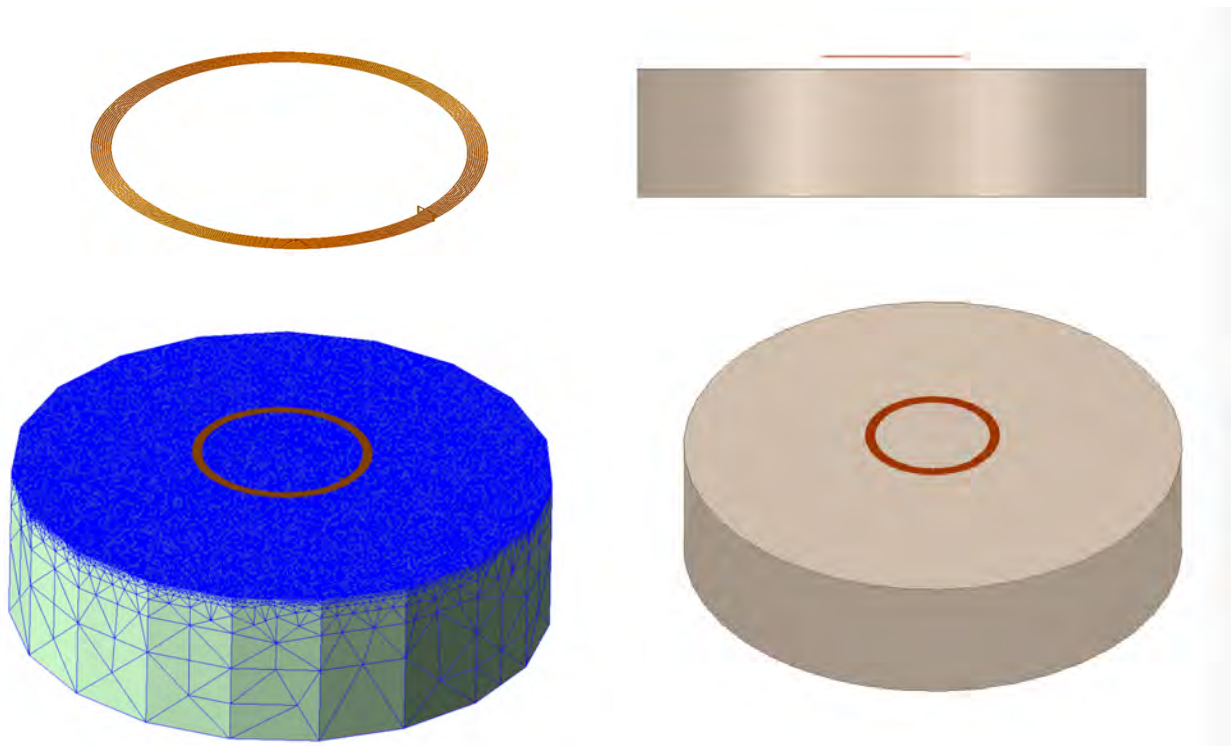
Figure 14: Current loop in front of a cuboid.

The simulated spatial peak RMS electric field in tissue is 1.55 V/m compared to the analytical 1.60 V/m.
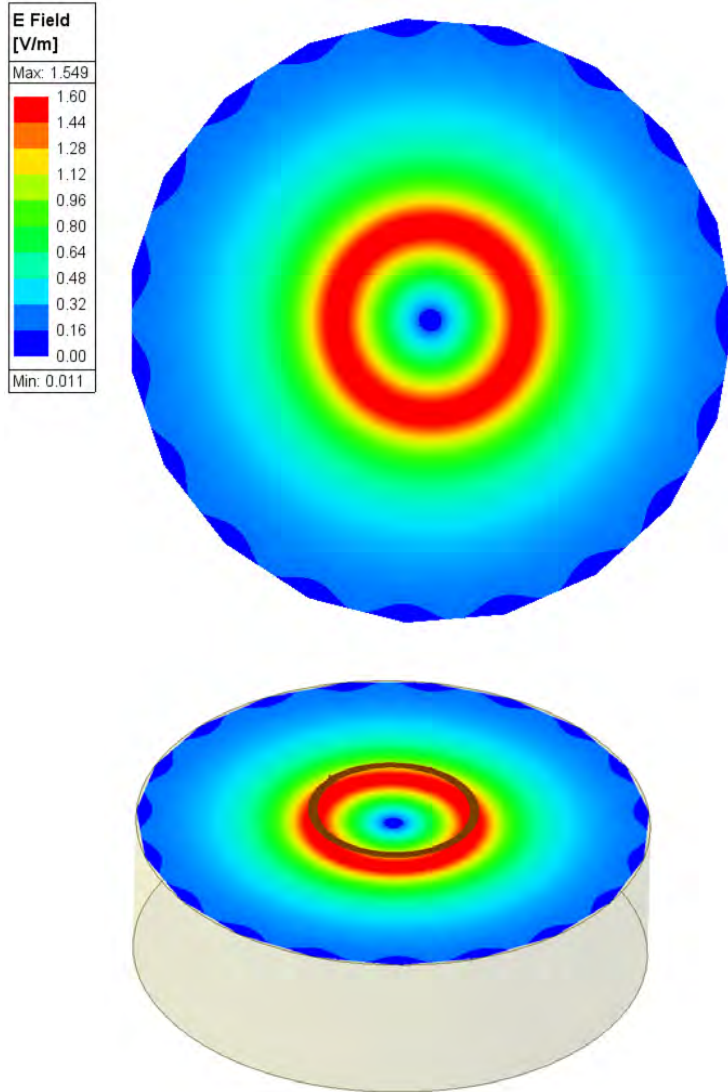
Figure 15: Electric Field plots at the phantom surface.

3) Computational peak SAR from peak components & One-gram averaged SAR procedure

The calculation method for SAR follows IEEE P1528.4. Once the solver calculated the S-Parameter results, different coils can be driven and the result from the S-Parameter calculation is automatically scaled to the driving current of the coils. This result combination provides the correctly scaled power loss density in the phantom. The SAR calculation computes the local SAR first using electric field and conducting current:

$$SAR = \vec{E} \bullet \vec{J}_{conj}/(2\rho)$$

Afterwards the local SAR is averaged over a specific mass, usually 1g or 10g. As described in [IEEE P1528.4] the mass averaging is done by mapping the results to a structured hexahedral grid and afterwards the averaging scheme for FDTD per [IEEE P1528.4] is applied. The SAR calculation on the hexahedral grid is compliant with IEC 62704-1.
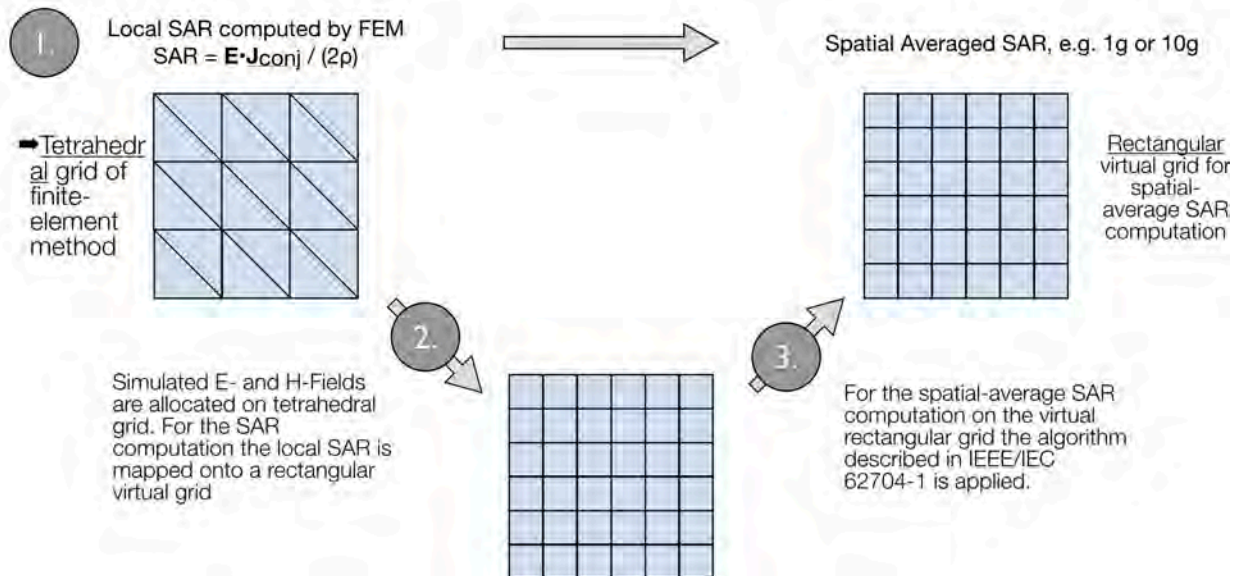
Figure 16: IEEE P1528.4 for SAR computation

4) Total Computational Uncertainty

Below is a table summarizing the budget of the uncertainty contributions of the numerical algorithm and of the rendering of the simulation setup. The table was filled using the IEC 62704-4, 2020. For the simulations, the extreme case where the phantom is placed directly in front of the Phone is considered. As the phantom with particular reference dielectric parameters are used (as described in section 5); the corresponding phantom dielectric uncertainty is set to zero (section 7.2.6, IEC 62704-4, 2020).

Table 11: Budget of uncertainty contributions of the numerical algorithm (filled based on IEC 62704-4 2020).

a	b	d	e	g
Uncertainty component	**Subclause**	**Probability distribution**	**Divisor f(d, h)**	**Uncertainty %**
Mesh resolution	7.2.2	N	1	**0.18**
ABC	7.2.3	N	1	**0.01**
Power budget	7.2.4	N	1	**0.01**
Convergence	7.2.5	R	1,73	**0.49**
Phantom dielectrics	7.2.5	R	1,73	**0.00**

Combined standard uncertainty ($k = 1$)	**0.69**

Below is a table summarizing the budget of the uncertainty of the developed model of the DUT so far. The table was filled using the IEC 62704-4, 2020.

Table 12: Uncertainty of DUT Model

a	b	d	e	g
Uncertainty component	**Subclause**	**Probability distribution**	**Divisor f(d, h)**	**Uncertainty %**
Uncertainty of the DUT model (based on near field distribution)	7.3.2	N	1	**0.69**
Uncertainty of the measurement equipment and procedure	7.3.3	N	1	**4.59**
Combined standard uncertainty ($k = 1$)				**5.28**

The expanded (K=2) uncertainty result as per the IEC/IEEE 62704-1, 2017 and IEC/IEEE 62704-4, 2020 is listed in Table 13. The expanded standard uncertainty is 10.56, which is lower than the limit of 30.

Table 13: Expanded Standard Uncertainty

a	b	c	d	e	f	g	h
Uncertainty component	**Sub clause**	**Tolerance %**	**Probability distribution**	**Divisor f(d,h)**	**c_i**	**Uncertainty %**	**v_i or v_{eff}**
Uncertainty of the test setup with respect to simulation parameters	7.2		N	1	1	0.69	
Uncertainty of the developed numerical model of the test setup	7.3		N	1	1	4.59	
Combined standard uncertainty ($k = 1$)						**5.28**	
Expanded standard uncertainty ($k = 2$)						**10.56**	

Columns c, g and h shall be filled in based on the results of Table 11 and Table 12

NOTE 1   Column headings a to h are given for reference

NOTE 2   Abbreviation used in Table 11:

  N – normal probability distribution

NOTE 3   The divisor is a function of the probability distribution and degrees of freedom (v_i and v_{eff})

NOTE 4 c_i is the sensitivity coefficient that is applied to convert the variability of the uncertainty component into a variability of SAR

The properties of the key materials of the DUT, as well as their tolerances, are listed in the following table.

Table 14: Material Properties and Tolerances

	Permittivity +/- Tolerance	Permeability +/- Tolerance	Loss Tangent +/- Tolerance	Conductivity +/- Tolerance
TX Ferrite	1	1345 +/-134	0	0
RX Ferrite	1	3300 +/-825	0	0
TX Coil	1	1	0	5.8e7 +/- 5.8e5
RX Coil	1	1	0	5.8e7 +/- 5.8e5
TX Shield	1	1	0	6.1e7 +/- 6.1e5
RX Shield	1	1	0	5.8e7 +/- 5.8e5

References:

1) IEC/IEEE 62704-4, 2020: "Determining the peak spatial-average specific absorption rate (SAR) in the human body from wireless communication devices, 30 MHz to 6 GHz – Part 4: General requirements for using the finite element method for SAR calculations."

2) IEC/IEEE 62704-1, 2017: "Determining the peak spatial-average specific absorption rate (SAR) in the human body from wireless communications devices, 30 MHz to 6 GHz - Part 1: General requirements for using the finite difference time-domain (FDTD) method for SAR calculations."

3) The electrical conductivity of human cerebrospinal fluid at body temperature, S.B. Baumann ; D.R. Wozny ; S.K. Kelly ; F.M. Meno, IEEE Transactions on Biomedical Engineering (Volume: 44 , Issue: 3 , March 1997)

4) https://itis.swiss/virtual-population/tissue-properties/database/thermal-conductivity/

5) C.Gabriel, S.Gabriel and E.Corthout: The dielectric properties of biological tissues: I. Literature survey, Phys. Med. Biol. 41 (1996), 2231-2249.

6) S.Gabriel, R.W.Lau and C.Gabriel: The dielectric properties of biological tissues: II. Measurements in the frequency range 10 Hz to 20 GHz, Phys. Med. Biol. 41 (1996), 2251-2269.

7) S.Gabriel, R.W.Lau and C.Gabriel: The dielectric properties of biological tissues: III. Parametric models for the dielectric spectrum of tissues, Phys. Med. Biol. 41 (1996), 2271-2293.

8) X. L. Chen et al., "Human Exposure to Close-Range Resonant Wireless Power Transfer Systems as a Function of Design Parameters," in IEEE Transactions on Electromagnetic Compatibility, vol. 56, no. 5, pp. 1027-1034, Oct. 2014.

9) http://hyperphysics.phy-astr.gsu.edu/hbase/magnetic/toroid.html